Journal of Science and Technology in Civil Engineering, HUCE, 2024, 18 (1): 39–54

STATIC AND DYNAMIC BEHAVIOUR OF SANDWICH BEAMS WITH POROUS CORE: EXPERIMENT AND MOVING LEAST SQUARES MESH-FREE ANALYSIS

Tran Quang Hung[a,c], Do Minh Duc[a,c,*], Tran Minh Tu[b,c], Le Xuan Dung[a], Chau Ngoc Bao[a]

[a] *Faculty of Civil Engineering, University of Science and Technology, The University of Danang, 54 Nguyen Luong Bang street, Lien Chieu district, Danang City, Vietnam*
[b] *Faculty of Building and Industrial Construction, Hanoi University of Civil Engineering, 55 Giai Phong road, Hai Ba Trung district, Hanoi, Vietnam*
[c] *Frontier Research Group of Mechanics of Advanced Materials and Structures (MAMS), HUCE, 55 Giai Phong road, Hai Ba Trung district, Hanoi, Vietnam*

Article history:
Received 18/12/2023, Revised 31/01/2024, Accepted 21/02/2024

Abstract

In this paper, the static and dynamic behaviour of sandwich beams with porous core are numerically analyzed and validated by experimental tests. The beam consists of a thick porous core with a uniform porosity distribution over its domain and two outer face layers. For the theoretical study, the virtual work principle is employed to derive the governing equation. A one-dimensional (1D) mesh-free approach, associated with the moving least squares Hermite interpolation, is developed to approximate the primary variable fields and discretize the governing equation. Additionally, a simple transformation method is applied to create Kronecker delta property of constructed shape functions, straightforwardly facilitating the imposition of the boundary condition, similar to the finite element method without additional techniques. The accuracy of the computational method is subsequently verified against previous literature. For the experimental tests, various mechanical responses, such as the natural frequency, static deflection, and deflection-time history of a cantilever porous sandwich beam consisting of cemboard faces and a concrete core with Expanded Polystyrene are measured and compared with the theoretical prediction. The outcomes of this study can be valuable for the design of sandwich beams with porous core.

Keywords: porous sandwich beam; expanded Polystyrene concrete; mesh-free method; moving least squares interpolation; natural frequencies; bending and vibration tests.

https://doi.org/10.31814/stce.huce2024-18(1)-04

1. Introduction

Sandwich structures, in which a porous core is embedded between two skin layers, are an ideal choice for constructing efficient lightweight structures. Each layer is responsible for its own role in the functioning of the structures. The two thin but strong face sheets resist the deflection, in-plane axial stress, and effect of external environment. The thick porous core connects the faces and resists the shear stress. The presence of porosity helps reduce self-weight, increase the ability of thermal and acoustic resistance as well as vibration absorption. Thanks to the mentioned advantages, these structures have found applications in various engineering areas, including building, transportation, aerospace, and military, etc. As an example, Fig. 1 illustrates an application of sandwich porous plates for a multi-story house.

Understanding in-depth the mechanical behaviour of structures is a significant task in designing and utilizing them. To achieve this, analyzing the mechanical responses of structures made of

*Corresponding author. *E-mail address:* ducdhbk@gmail.com (Duc, D. M.)

(a) Sandwich plate with Expanded Polystyrene (EPS) concrete core

(b) A multi-story house made of EPS concrete sandwich plates

Figure 1. Applications of sandwich porous plates

novel materials has required efforts from scientists and engineers. Various reports on these topics, especially porous sandwich structures and beams, have been published recently. For example, Chen et al. [1] focused on the nonlinear free vibration of sandwich beams with porous core using Ritz method associated with Timoshenko beam theory (TBT) and von Kármán geometric nonlinearity assumption. Based on Chebyshev–Ritz method, Wang et al. [2] studied the nonlinear bending behaviour of sandwich beams with a metal foam (a metal porous material) core and two composite face sheets reinforced with graphene platelets (GPLs). Srikarun et al. [3] investigated the linear and nonlinear static bending of sandwich beams with porous core and homogeneous face sheets by Ritz method. Magnucka-Blandzi [4] presented the analysis of dynamic stability of simply supported sandwich beams with a metal foam core by analytical solution. Wang and Zhao [5] studied the natural frequencies of sandwich beams with a metal foam core resting on Pasternak foundation by Chebyshev collocation method. Garg et al. [6] presented the free vibration and static bending of sandwich beams with a metal foam core using finite element method (FEM). Recently, using functionally graded materials (FGMs) for the face sheets to promote their excellent features, such as high strength and moduli, good weather and thermal resistance, has been proposed. The mechanical behaviour of sandwich porous beams with FGM faces has been reported in various papers, e.g., [7–11].

Besides theoretical studies, many authors have concerned about experimental tests to have an actual view and confirm the reliability for application. For example, Jasion et al. [12] performed theoretical and experimental studies of the global and local buckling–wrinkling of the face sheets of sandwich beams and sandwich circular plates with metal foam core. Sokolinsky et al. [13] carried out four-point bending tests and analytical study of sandwich beams with aluminum face sheets and a Divinycell foam core. The work in Ref. [13] was extended to the free vibration problem by Sokolinsky et al. [14]. Dariushi and Sadighi [15] investigated the geometrically nonlinear bending of sandwich beams with glass/epoxy face sheets and soft polymeric core by analytical predictions and experimental tests. Njim et al. [16] conducted a three-point bending test for 3D printed sandwich beams with porous core bonded with aluminum face sheets to measure the peak load and maximum deflection. In [16], the experimental results were compared with those of numerical prediction by FEM.

The literature review reveals that all the mentioned reports focused on exploring mechanical behaviour, developing theoretical and experimental models, and investigating the effects of assumptions on the results. However, sandwich structures with porous core represent a novel and modern form of

lightweight structures, and theoretical studies to simulate and investigate their mechanical behaviour are limited. In addition, experimental studies on these structures are rare compared to theoretical ones. Therefore, significant research effort is needed to comprehend their behaviour for effective applications. The literature survey also shows that various computation methods have been developed for simulating the mechanical behaviour of these structures. Nevertheless, developing a novel and robust computation tool still needs in order to enhance the effectiveness of simulation.

The current study will contribute two significant aspects: (i) developing for the first time a moving least squares mesh-free method in which a 1D Hermite interpolation is adopted to construct the shape functions for approximation of the displacement field to simulate mechanical behaviour of porous sandwich beams; (ii) doing experiments on a porous sandwich beam to validate the simulated results and give a view on its actual behaviour.

This paper is devoted to analyzing the static bending and vibration of sandwich beams with a porous core using both theoretical and experimental approaches. The structure of the beam includes a uniform porosity distribution porous core covered by two homogeneous face layers. For the theoretical study, the virtual work principle is employed to derive the governing equation. A 1D mesh-free approach, which is based on the moving least squares Hermite interpolation to approximate the primary variable fields, is developed to discretize the governing equation. A simple transformation technique is used to create Kronecker delta property of the shape functions which helps impose the essential boundary condition directly as the conventional FEM without additional techniques. The accuracy of the computational method is verified by comparison to earlier publishes. For the experimental tests, some mechanical responses, such as the fundamental natural frequency, static deflection, deflection-time history of a cantilever porous sandwich beam with Expanded Polystyrene-based concrete core are performed and compared with those of the theoretical predictions.

2. Theory and formulations

Consider a porous sandwich beam with dimensions $L \times b \times h$ as illustrated in Fig. 2. The x-axis lies on the mid-plane of the beam, and the z-axis is taken upward direction. The thicknesses of the core and face layers are h_c and h_f, respectively ($h = h_c + 2{\times}h_f$). The developed theory is based on two assumptions: (i) the face sheets and the core are made of linearly elastic materials, and (ii) no relative sliding between them.

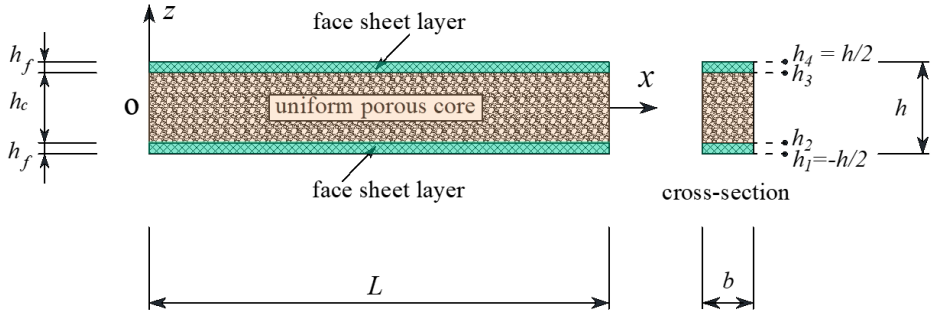

Figure 2. Porous sandwich beam and geometrical parameters

2.1. *Effective material property modelling*

In this work, the material of the face layers is isotropic. Their mechanical properties, i.e., elastic moduli E and G, mass density ρ, and Poisson's ratio ν are constant, whereas those of porous material

depend on the porosity. In the case of the uniform porosity distribution, they can be expressed as functions of porosity coefficient as follows [1]

$$\begin{cases} E(z) = E_1(1 - e_0) \\ G(z) = E(z)/(2 + 2\nu) \\ \rho(z) = \rho_1(1 - e_m) \\ -h_c/2 \le z \le h_c/2 \end{cases} \tag{1}$$

where e_0 is the porosity coefficient which is defined as [1]

$$e_0 = 1 - E_2/E_1 \tag{2}$$

In Eqs. (1) and (2), E_1 and E_2 are Young's moduli of material without and with porosity, respectively.

The coefficient of mass density is defined as [1]

$$e_m = 1 - \rho_2/\rho_1 \tag{3}$$

where ρ_1 and ρ_2 are the mass densities of material without and with porosity, respectively.

The relation between Young's modulus and the mass density of porous materials can be expressed as [1, 17]

$$\begin{cases} E_2/E_1 = (\rho_2/\rho_1)^2 & \text{for open - cell} \\ E_2/E_1 = \left(\dfrac{\rho_2/\rho_1 + 0.121}{1.121}\right)^{2.3} & \text{for closed - cell} \end{cases} \tag{4}$$

Eqs. (2), (3) and (4) deduce the relation between e_0 and e_m as

$$\begin{cases} e_m = 1 - \sqrt{1 - e_0} & \text{for open - cell} \\ e_m = 1.121\left(1 - \sqrt[2.3]{1 - e_0}\right) & \text{for closed - cell} \end{cases} \tag{5}$$

2.2. *Displacement, strain and stress fields*

In the current study, the third-order beam theory (TOBT) [3, 18] is employed. Based on TOBT, the displacement components $u(x, z, t)$, $w(x, z, t)$, which are, respectively, along the x- and z-directions, can be written as

$$\begin{cases} \mathbf{d} = \begin{Bmatrix} u(x,z,t) \\ w(x,z,t) \end{Bmatrix} = \underbrace{\begin{bmatrix} 1 & 0 & -z & \xi(z) \\ 0 & 1 & 0 & 0 \end{bmatrix}}_{\mathbf{\Theta}_1} \mathbf{A}_1 = \mathbf{\Theta}_1 \mathbf{A}_1 \\ \xi(z) = z - 4z^3/\left(3h^2\right) \\ \mathbf{A}_1^T = \{u_0(x,t)\, w_0(x,t)\, w_{0,x}(x,t)\, \phi_0(x,t)\}, \end{cases} \tag{6}$$

where u_0, w_0 and φ_0 are the axial displacement, transverse displacement and the transverse shear strain on the mid-plane (i.e., $z = 0$), respectively. They are three primary variable functions of the problem, t denotes the time.

The strain-field is derived from the displacement field by

$$\begin{cases} \boldsymbol{\varepsilon} = \begin{Bmatrix} \varepsilon_x \\ \gamma_{xz} \end{Bmatrix} = \underbrace{\begin{bmatrix} 1 & -z & \xi(z) & 0 \\ 0 & 0 & 0 & \xi'_z(z) \end{bmatrix}}_{\mathbf{\Theta}_2} \mathbf{A}_2 = \mathbf{\Theta}_2 \mathbf{A}_2 \\ \mathbf{A}_2^T = \{u_{0,x} w_{0,xx} \phi_{0,x} \phi_0\} \end{cases} \tag{7}$$

The stress-strain relationships obey Hook's law and can be written as

$$\boldsymbol{\sigma} = \left\{ \begin{array}{c} \sigma_x \\ \tau_{xz} \end{array} \right\} = \underbrace{\left[\begin{array}{cc} E(z)/\left(1-\nu^2\right) & 0 \\ 0 & G(z) \end{array} \right]}_{\mathbf{E}_b} \boldsymbol{\varepsilon} = \mathbf{E}_b \boldsymbol{\varepsilon} \tag{8}$$

In Eqs. (6) and (7), the notations $(\bullet)_{,x}$ and $(\bullet)_{,xx}$ imply the first and second derivatives of $(\bullet)$ with respect to x, respectively; $(\bullet)_{,z}$ implies the first derivative of $(\bullet)$ with respect to z. The superscript $(\bullet)^T$ implies the operation of matrix transposition.

2.3. Energy expressions

The virtual variation of internal energy (δU) of the beam can be expressed as follows

$$\delta U = \int_V \boldsymbol{\sigma}^T \delta\boldsymbol{\varepsilon} dV = \int_V \boldsymbol{\varepsilon}^T \mathbf{E}_b \delta\boldsymbol{\varepsilon} dV \tag{9}$$

By substituting the strains from Eq. (7) into Eq. (9), the virtual variation of internal energy can be described as

$$\delta U = \int_0^L \mathbf{A}_2^T \mathbf{H}_E \delta\mathbf{A}_2 dx \tag{10}$$

where $\mathbf{H}_E$ is the matrix of stiffness coefficients which is defined as

$$\mathbf{H}_{E(4\times4)} = b \int_{-0.5h}^{0.5h} \boldsymbol{\Theta}_2^T \mathbf{E}_b \boldsymbol{\Theta}_2 dz \tag{11}$$

The virtual variation of external work (δS) done by the applied load $q_0(x,t)$ and concentrated load Q at coordinate x_P can be expressed as

$$\delta S = -\int_0^L q_0(x,t)\,\delta w_0(x,t)\,dx - Q\delta w_0(x_P,t) \tag{12}$$

The virtual variation of the kinetic energy of the beam can be expressed as follows

$$\delta K = \int_V \rho(z)\,\ddot{\mathbf{d}}^T \delta\mathbf{d} dV \tag{13}$$

Substituting the displacements from Eq. (6) into Eq. (13), the virtual variation of the kinetic energy can be described as

$$\delta K = \int_0^L \ddot{\mathbf{A}}_1^T \mathbf{H}_R \delta\mathbf{A}_1 dx \tag{14}$$

In Eqs. (13) and (14), the two over dots $(\ddot{\bullet})$ indicate second derivative of $(\bullet)$ with respect to time; $\mathbf{H}_R$ is a matrix of size 4×4 depending on $\rho(z)$. It is defined as

$$\mathbf{H}_{R(4\times4)} = b \int_{-0.5h}^{0.5h} \boldsymbol{\Phi}_1^T \rho(z)\,\boldsymbol{\Phi}_1 dz \tag{15}$$

The virtual work principle for the system can be stated as follows to derive the governing equation [19]

$$\delta U + \delta K + \delta S = 0 \tag{16}$$

2.4. Mesh-free approach

There are various computational methods that have been developed for simulating the mechanical behaviour of structures. However, there is still a need to develop a novel and robust computational tool to enhance the effectiveness of mechanical model. Mesh-free method (MFM) is the next generation of numerical ones beyond FEM [20]. 1D MFM based on the point interpolation and polynomial basis proves its effectiveness for modelling sandwich beams in previous works [8, 21–23]. To enrich computational models, 1D MFM with moving least squares (MLS) Hermite interpolation will be developed in this study.

The MFM using the MLS interpolation was first proposed by Belytschko et al. [24]. Although the limitation of the method is the MLS shape functions do not have the Kronecker delta function property [20, 25, 26], this method is gradually becoming a mature and practical computational approach in the field of computational mechanics [26]. This is due to the stability in the function approximation and the discretized global system equations [26]. On the other hand, the Kronecker delta function property for the MLS shape functions can be easily recovered by using the simple transformation technique, which was proposed by Atluri et al. [27].

Note that the MFM which is based on the point interpolation using polynomial or radial basis functions possesses the Kronecker delta function property of the shape functions [20, 26].

a. Moving least squares interpolation for approximation of the displacement field

Consider a support domain Ω_s at a point of interest [20], which is a subdomain of the beam domain Ω. Distribute arbitrarily N nodes along the x-axis in Ω_s (1D modelling). A function $\hat{u}_0(x,t)$, which is represented for the displacement fields $u_0(x,t)$, $w_0(x,t)$ and $\varphi_0(x,t)$ within the support domain Ω_s, can be approximated based on the MLS interpolation [24, 28] as

$$\hat{u}_0(x,t) \simeq \hat{u}_0^h(x,t) = \sum_{i=1}^{M} p_i(x) a_i(x,t) = \mathbf{p}^T(x)\,\mathbf{a}(x,t) \tag{17}$$

where $\hat{u}_0^h(x,t)$ is the approximate function of $\hat{u}_0(x,t)$; $\mathbf{p}^T(x)$ is the vector of monomial basis functions, which can have the common form for 1D interpolation as follows

$$\mathbf{p}^T(x) = \left\{1, x, x^2, \ldots, x^{(M-1)}\right\} \tag{18}$$

where M is the number of terms in the basis; $\mathbf{a}(x,t)$ is the vector of unknown coefficients which depends on coordinate x and time t

$$\mathbf{a}(x,t) = \{a_1(x,t), a_2(x,t), \ldots, a_M(x,t)\}^T \tag{19}$$

In this study, Hermite interpolation type [29], which uses both the values of function and its first derivative at the nodes (nodal coordinate), is adopted. Basing on this interpolation type, the coefficients $a_i(x,t)$ are determined by minimizing a functional $J(x,t)$ defined as [28]

$$J(x,t) = \sum_{I=1}^{N} w_I(x,t)\left[\mathbf{p}^T(x_I,t)\,\mathbf{a}(x,t) - u_I\right]^2 + \sum_{I=1}^{N} w_I(x,t)\left[\mathbf{p}_{,x}^T(x_I,t)\,\mathbf{a}(x,t) - \theta_I\right]^2 \tag{20}$$

in which, x_I is the coordinate of node I in the support domain Ω_s; u_I, θ_I represent the nodal parameters for node I (they are actually not the nodal values of function $\hat{u}_0(x,t)$ for node I, i.e., $\hat{u}_0(x_I,t)$ and $\hat{u}_{0,x}(x_I,t)$, respectively); $w_I(x)$ denotes the weight function associated with node I such that $w_I(x) \geq 0$ for all x in the support domain Ω_s of $w_I(x)$ and zero otherwise.

The matrix form of Eq. (20) can be expressed as

$$J(x,t) = \left[\left\{\begin{array}{c}\mathbf{P}\\ \mathbf{P}_x\end{array}\right\}\mathbf{a}(x,t) - \left\{\begin{array}{c}\mathbf{u}\\ \theta\end{array}\right\}\right]^T \left[\begin{array}{cc}\mathbf{W} & 0\\ 0 & \mathbf{W}\end{array}\right]\left[\left\{\begin{array}{c}\mathbf{P}\\ \mathbf{P}_x\end{array}\right\}\mathbf{a}(x,t) - \left\{\begin{array}{c}\mathbf{u}\\ \theta\end{array}\right\}\right] \tag{21}$$

where

$$\mathbf{u}^T = \{u_1, u_2, \ldots, u_N\}; \theta^T = \{\theta_1, \theta_2, \ldots, \theta_N\} \tag{22}$$

$$\mathbf{W} = \left[\begin{array}{cccc} w_1 & 0 & 0 & 0\\ 0 & w_2 & 0 & 0\\ 0 & 0 & \ldots & 0\\ 0 & 0 & 0 & w_N\end{array}\right]_{N\times N} \tag{23}$$

$$\mathbf{P}^T = \left\{\mathbf{p}^T(x_1), \mathbf{p}^T(x_2), \ldots, \mathbf{p}^T(x_N)\right\}; \quad \mathbf{P}_x^T = \left\{\mathbf{p}_{,x}^T(x_1), \mathbf{p}_{,x}^T(x_2), \ldots, \mathbf{p}_{,x}^T(x_N)\right\} \tag{24}$$

The stationarity of the functional $J(x,t)$ with respect to the coefficients $\mathbf{a}(x,t)$ leads to the following relation [28]:

$$\mathbf{A}(x)\mathbf{a}(x,t) = \mathbf{C}(x)\mathbf{q}_{\Omega_s}(t) \tag{25}$$

where

$$\mathbf{A}(x) = \mathbf{P}^T\mathbf{W}\mathbf{P} + \mathbf{P}_x^T\mathbf{W}\mathbf{P}_x \tag{26}$$

$$\mathbf{C}(x) = \left\{\mathbf{P}^T\mathbf{W}, \mathbf{P}_x^T\mathbf{W}\right\} \tag{27}$$

$$\mathbf{q}_{\Omega_s}(t) = \{\mathbf{u}\theta\}^T = \{u_1, u_2, \ldots, u_N, \theta_1, \theta_2, \ldots, \theta_N\}^T \tag{28}$$

From Eq. (25), the vector of coefficients $\mathbf{a}$ is determined by

$$\mathbf{a}(x,t) = \mathbf{A}^{-1}(x)\mathbf{C}(x)\mathbf{q}_{\Omega_s}(t) \tag{29}$$

By substituting back vector $\mathbf{a}$ from Eq. (29) into Eq. (17), leading to

$$\hat{u}_0^h(x,t) = \mathbf{p}^T(x)\mathbf{a}(x,t) = \mathbf{p}^T(x)\mathbf{A}^{-1}(x)\mathbf{C}(x)\mathbf{q}_{\Omega_s}(t) = \boldsymbol{\eta}(x)\mathbf{q}_{\Omega_s}(t) \tag{30}$$

In Eq. (30) $\boldsymbol{\eta}(x)$ is the vector of nodal shape functions of approximated function $\hat{u}_0^h(x,t)$ which is determined by

$$\boldsymbol{\eta}(x) = \mathbf{p}^T(x)\mathbf{A}^{-1}(x)\mathbf{C}(x) \tag{31}$$

b. Weight function

In the MLS approximation, there are various kinds of weight functions that can be adopted. In this work, the weight function proposed by Atluri [28] in the following equation is employed

$$w_I(x) = \left\{\begin{array}{ll}\left(1 - \|x - x_I\|^2/R_I^2\right)^3 & \|x - x_I\| \leq R_I\\ 0 & \|x - x_I\| > R_I\end{array}\right. \tag{32}$$

where $R_I = \alpha \times d_s$, denotes the radius of support domain of the weight function; d_s is the average nodal spacing in the support domain Ω_s; α is the scaling parameter.

c. Transformation technique

Due to the feature of MLS interpolation, the approximated function does not pass through the nodal data, i.e., $\mathbf{q}_{\Omega_s}$ of Eq. (28), which is used to interpolate it. For this reason, the nodal data $\mathbf{q}_{\Omega_s}$ are also called fictitious values [28] at nodes. This leads to the constructed shape functions do not satisfy the Kronecker delta property and the essential boundary conditions cannot be imposed directly [27].

To overcome the drawback, a simple transformation technique was proposed by Atluri et al. [27] to transform the fictitious nodal values $\mathbf{q}_{\Omega_s}$ to the actual nodal values $\hat{\mathbf{q}}_{\Omega_s}$. Following is the procedure.

From the approximated function $\hat{u}_0^h(x,t)$, Eq. (30), the values of this function at node K with the coordinate x_K can be calculated by

$$\begin{cases} \hat{u}_K = \hat{u}_0^h(x_K,t) = \boldsymbol{\eta}(x_K)\,\mathbf{q}_{\Omega_s} \\ \hat{\theta}_K = \hat{u}_{0,x}^h(x_K,t) = \boldsymbol{\eta}_{,x}(x_K)\,\mathbf{q}_{\Omega_s} \end{cases} \tag{33}$$

Carrying out for all the N nodes in the support domain Ω_s, we have

$$\begin{cases} \hat{u}_1 = \boldsymbol{\eta}(x_1)\,\mathbf{q}_{\Omega_s} \\ \hat{u}_2 = \boldsymbol{\eta}(x_2)\,\mathbf{q}_{\Omega_s} \\ \dots \\ \hat{u}_N = \boldsymbol{\eta}(x_N)\,\mathbf{q}_{\Omega_s} \end{cases} \quad \begin{cases} \hat{\theta}_1 = \boldsymbol{\eta}_{,x}(x_1)\,\mathbf{q}_{\Omega_s} \\ \hat{\theta}_2 = \boldsymbol{\eta}_{,x}(x_2)\,\mathbf{q}_{\Omega_s} \\ \dots \\ \hat{\theta}_N = \boldsymbol{\eta}_{,x}(x_N)\,\mathbf{q}_{\Omega_s} \end{cases} \tag{34}$$

The matrix form of Eq. (34) can be written as

$$\hat{\mathbf{q}}_{\Omega_s} = \left\{\hat{u}_1\ \hat{u}_2\ \dots\ \hat{u}_N\ \hat{\theta}_1\ \hat{\theta}_2\ \dots\ \hat{\theta}_N\right\}^T = \mathbf{R}\mathbf{q}_{\Omega_s} \tag{35}$$

$$\mathbf{R} = \left\{\boldsymbol{\eta}(x_1)\ \ \boldsymbol{\eta}(x_2)\ \dots\ \boldsymbol{\eta}(x_N)\ \ \boldsymbol{\eta}_{,x}(x_1)\ \ \boldsymbol{\eta}_{,x}(x_2)\ \dots\ \boldsymbol{\eta}_{,x}(x_N)\right\}^T \tag{36}$$

Eq. (35) expresses the relation between the actual nodal values $\hat{\mathbf{q}}_{\Omega_s}$ (function values) and the fictitious nodal values $\mathbf{q}_{\Omega_s}$ of the nodes in the support domain Ω_s.

By inverting Eq. (35), we have:

$$\mathbf{q}_{\Omega_s} = \mathbf{R}^{-1}\hat{\mathbf{q}}_{\Omega_s} \tag{37}$$

where $\mathbf{R}^{-1}$ is called transformation matrix [27].

Substituting back Eq. (37) into Eq. (30) results in the approximated function $\hat{u}_0^h(x,t)$, which expressed through the actual nodal values $\hat{\mathbf{q}}_{\Omega_s}$

$$\hat{u}_0(x,t) = \boldsymbol{\eta}(x)\,\mathbf{q}_{\Omega_s} = \boldsymbol{\eta}(x)\,\mathbf{R}^{-1}\hat{\mathbf{q}}_{\Omega_s} = \boldsymbol{\Xi}(x)\,\hat{\mathbf{q}}_{\Omega_s} \tag{38}$$

where $\boldsymbol{\Xi}(x)$ is the matrix of constructed shape functions of $\hat{u}_0^h(x,t)$ which is modified from matrix $\boldsymbol{\eta}(x)$ so that the function values coincide with the actual nodal values. This means that constructed shape functions satisfy the Kronecker delta property. The matrix can be written in the explicit form as

$$\boldsymbol{\Xi}(x) = \left\{\Xi^{(1)}\ \Xi^{(2)}\ \dots\ \Xi^{(N)}\ \Xi_\theta^{(1)}\ \Xi_\theta^{(2)}\ \dots\ \Xi_\theta^{(N)}\right\}_{1\times 2N} = \boldsymbol{\eta}(x)\,\mathbf{R}^{-1} \tag{39}$$

Substituting back Eq. (39) into Eq. (38) leads to:

$$\hat{u}_0(x,t) = \boldsymbol{\Xi}(x)\,\hat{\mathbf{q}}_{\Omega_s} = \left\{\Xi^{(1)}\ \Xi^{(2)}\ \dots\ \Xi^{(N)}\ \Xi_\theta^{(1)}\ \Xi_\theta^{(2)}\ \dots\ \Xi_\theta^{(N)}\right\}\hat{\mathbf{q}}_{\Omega_s} \tag{40}$$

d. Discrete formulations

Dividing the beam into a set of non-overlapping sub-domains which are called background cells [26]. Because each of background cell (e.g., Ω_c) can be pertain to an influence domain (e.g., Ω_s). Therefore, the field variables in Ω_c is also the field variables in Ω_s which are approximated by Eq. (40). Hence, by substituting Eq. (40) into Eqs. (10), (12), and (14), the energies are then expressed through the unknown nodal values. After that, applying the virtual work principle, i.e., Eq. (16), the governing equation for problem in the domain Ω_c is discretized into a set of algebraic equations with the matrix form as

$$\mathbf{M}_{\Omega_c}\ddot{\mathbf{U}}_{\Omega_s} + \mathbf{K}_{\Omega_c}\mathbf{U}_{\Omega_s} = \mathbf{F}_{\Omega_c} \tag{41}$$

where $\mathbf{M}_{\Omega_c}$ is the mass matrix, $\mathbf{K}_{\Omega_c}$ the stiffness matrix, and $\mathbf{F}_{\Omega_c}$ is the load vector; $\mathbf{U}_{\Omega_s}$ is the vector collecting all the nodal values of all the field variables in the influence domain Ω_s, which has the form of

$$\mathbf{U}_{\Omega_s} = \left\{ \begin{array}{cccccccc} u_{01} & u_{01}^{\bullet} & w_{01} & w_{01}^{\bullet} & \varphi_{01} & \varphi_{01}^{\bullet} & \cdots & \\ & & \cdots & u_{0N} & u_{0N}^{\bullet} & w_{0N} & w_{0N}^{\bullet} & \varphi_{0N} \quad \varphi_{0N}^{\bullet} \end{array} \right\}^T_{(1\times 6N)} \tag{42}$$

In Eq. (42), $(\bullet)_i$ and $(\bullet)_i^{\bullet}$, respectively, stand for the values of the field variable $(\bullet)$ and its first derivative at i-th node. Due to the beam is modeled with three displacement fields, there are a total of six degrees of freedom per node.

For the whole problem domain, the system of global discrete equations is formed by assembling Eq. (41) for all the background cells

$$\mathbf{M}\ddot{\mathbf{U}} + \mathbf{K}\mathbf{U} = \mathbf{F} \tag{43}$$

where $\mathbf{M}$ is the global mass matrix, $\mathbf{K}$ is the global stiffness matrix, $\mathbf{F}$ is the global load vector, $\mathbf{U}$ is the global nodal value vector.

In general, the procedure to results in the discrete governing equations, i.e., (41) and (43), is similar to the one applied for the standard FEM.

3. Convergence study theoretical validation

This section is devoted to verifying the convergence and correctness of the established mathematical solution. Both the convergence and validation are conducted in each numerical example for convenience. Two examples, selected from the studies of Chen et al. [1] for free vibration and of Srikarun et al. [3] for static bending, are illustrated. The sandwich beams consist of two steel face sheets and a steel foam core which is the open-cell foam. Material properties are: $E_f = E_1 = E_{steel}$ = 200 GPa, $\rho_f = \rho_1 = \rho_{steel}$ = 7850 kg/m^3, Poisson's ratio is constant, $\nu = \nu_{steel}$ = 1/3 [1]. Subscript $(\bullet)_f$ denotes the face sheets. Two typical types of boundary edge for the beam are considered. They are clamped-clamped (CC), simply-supported (SS) edges. The deflection and fundamental natural frequency of the beam are considered. Their dimensionless forms are used to present the results as follows [1, 3].

$$\hat{w}(x) = w(x)/h; \quad \hat{\omega} = \omega L\sqrt{\rho_{steel}\left(1-\nu_{steel}^2\right)/E_{steel}} \tag{44}$$

To compatibility with the studies of Chen et al. [1] and of Srikarun et al. [3] for comparison purpose, the porosity coefficient e_0 in Eqs. (1) and (5) needs to be replaced by $e_0^* \times \chi$, $\chi = \dfrac{1}{e_0^*} - \dfrac{1}{e_0^*}\left(\dfrac{2}{\pi}\sqrt{1-e_0^*} - \dfrac{2}{\pi} + 1\right)^2$ [3]. This is because the study of Chen et al. [1] and of Srikarun et al. [3] defined e_0^* for the case of symmetric/asymmetric porosity distribution with the cosine rule. Then, for

the case of uniform porosity distribution, the porosity coefficient is deduced by multiplying e_0^* by χ to satisfy the equivalent mass condition of the beams with the different types of porosity distribution.

Throughout the mesh-free analysis, the uniform nodal distribution along the beam is adopted for convenience. The scaling parameter (α) to determine the radius of the support domain for constructing the shape functions as well as for the weight function is chosen to be 3 times the nodal spacing (4-6 nodes per domain). This parameter is recommended to be from 2.0 to 3.0 [20, 26]. The number of terms M in the basis is taken to be 3. M must not be larger than the number of nodes in the support domain to ensure the existence of a well-conditioned matrix for constructing the shape functions [20, 26]. These two parameters (α and M) should be assumed by the analyst before analyzing and then determined appropriately by carrying out the numerical experiments. Besides, four-point Gauss quadrature scheme is selected to compute the matrices $\mathbf{M}_{\Omega_c}$, $\mathbf{K}_{\Omega_c}$ and vector $\mathbf{F}_{\Omega_c}$.

The results presented in Tables 1 and 2 show that the MLS mesh-free analysis with Hermite interpolation achieves a fast convergence rate; the solution can converge to 6 digits after the decimal point within the 21-node scheme. In addition, the current results completely agree with those of Chen et al. [1] and of Srikarun et al. [3].

Table 1. Convergence and theoretical validation of $\hat{\omega}_1$ ($e_0^* = 0.5$, $h_c/h_f = 10$, $L/h = 20$)

BCs	Number of nodes					[1]
	5	11	21	31	41	
SS	0.1383	0.1383	0.1383	0.1383	0.1383	0.1383
CC	0.3100	0.3084	0.3083	0.3083	0.3083	0.3084

Table 2. Convergence and validation of $\hat{w}\,(L/2)$ ($L = 1$ m, $h = b = 0.1$ m, $e_0^* = 0.5$, $h_c/h_f = 8$)

BCs	Number of nodes					[3]
	5	11	21	31	41	
SS	0.004337	0.004343	0.004343	0.004343	0.004343	0.004343
CC	0.000970	0.000978	0.000980	0.000980	0.000980	0.000980

4. Experimental tests and validation

4.1. Specimen preparation

One beam specimen whose dimensions ($L \times b \times h$) are (1200×206×90) mm, within ± 0.5 mm tolerances, are cut from an Expanded Polystyrene (EPS) concrete sandwich panel supplied by NUCE wall manufacturer. The two outer layers of the panel are the cement cemboards and the porous light weight core is the concrete with EPS which has closed-cellular structure [30]. The thickness of the core (h_c) and each face sheet (h_f) are: $h_c = 80$ mm and $h_f = 5$ mm, respectively. Material properties of the cemboard include: mass density $\rho = 1260$ kg/m^3, Young's modulus $E = 4500$ MPa. Young's modulus of the EPS concrete core $E = E_2 = 3349$ MPa. The properties are supplied by NUCE wall manufacturer. Poisson's ratio (ν) of the materials is assumed equal to 0.3. The sandwich beam specimen with a porous core is shown in Fig. 3.

The concrete matrix is the mortar grade M100 with Young's modulus $E_1 = 14500$ MPa and mass density $\rho_1 = 1800$ kg/m^3. Using Eq. (2) and the relation of Eq. (5), the porosity coefficient and the coefficient of mass density of EPS concrete core can, respectively, be calculated: $e_0 = 0.7690$ and $e_m = 0.5282$. Thus, using Eq. (1), the mass density of EPS concrete core is determined as $\rho = \rho_2 = 849.26$ kg/m^3.

Figure 3. Sandwich beam specimen

4.2. Procedure setup

The test beam is conducted for the case of cantilever beam with clamped-free (CF) edges. This beam type is selected because it is a simple mechanical model to install as well as basis for complex structures. In addition, measured values of the beam are easier to set up to stay in the measuring range of the device of the laboratory than the beams with other boundary conditions. 200 mm length of the test beam is spent to fix to the pedestal.

Figure 4. Graphical user interface of the DCS-100A software

Two types of tests are conducted for some primary mechanical behaviour. The first one is to investigate the flexural bending via the deflection under static load. The second one is to examine the fundamental frequency and deflection-time history. The position to measure the deflection is in the distance 100 mm from the free end. For static tests, ten step incremental loads are applied from the initial load of 5 kG (5×9.81 N) with the increment of 1 kG (9.81 N) per step. Data are recorded at each step load after the deflection is in stable condition. For the vibration test, the beams are excited by a rubber hammer (in the vertical direction) or cutting a 10 kG (10×9.81 N) weight hanging by a string at the same position of the static test. Note that, for the fundamental frequency test, the excited position may be freely to choose.

A linear variable displacement transducer (LVDT) is placed on the top mid-surface and 100 mm from the free end. In addition, an accelerometer is installed on the free end of the beam to record the acceleration. Both the LVTD and accelerometer are KYOWA's product. The displacement range of LVTD is up to 50 mm, and the frequency range of the accelerometer is from 0 to 70 Hz. The two

devices are connected to a personal computer through EDX-10A/B using the DCS-100A software of KYOWA. The DAS-200A data analyzing software, of KYOWA, is also integrated with the computer to convert the analog into digital signals and transform them into frequency domain by Fast Fourier Transform (FFT). The graphical user interface of the DCS-100A software is shown in Fig. 4. The schematic of the tests is illustrated in Fig. 5. The installed beam is shown in Fig. 6.

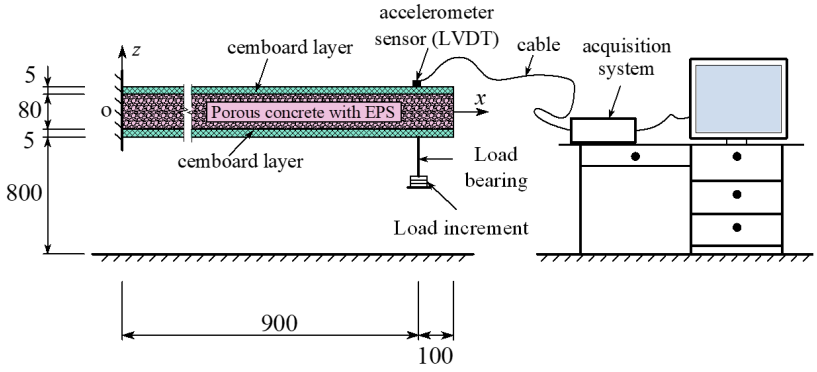

Figure 5. Schematic of the tests (unit of length: mm)

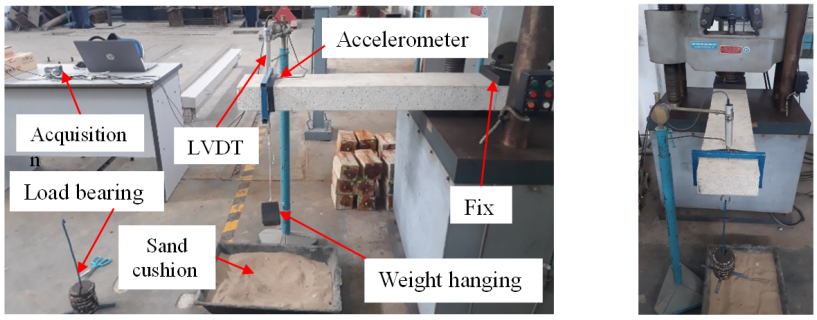

Figure 6. Installed beam and devices

4.3. Experimental results and mesh-free prediction

a. Static bending

The measurement results of three sets of the test for the beam under different applied load levels and comparison with the theoretical prediction are presented in Table 3 and plotted in Fig. 7. In the presentation, the downward deflection is positive.

Table 3. Static deflection (mm) at $x = 0.9$ (m) from the left end ($P = 9.81$ N)

Test/theoretical prediction	Applied loads				
	$6\times P$	$8\times P$	$10\times P$	$12\times P$	$14\times P$
1^{st} measurement	0.2530	0.3510	0.4420	0.5290	0.6250
2^{nd} measurement	0.2598	0.3623	0.4527	0.5409	0.6341
3^{rd} measurement	0.2619	0.3582	0.4520	0.5410	0.6364
Average	0.2582	0.3572	0.4489	0.5369	0.6319
Theoretical prediction	0.2843	0.3791	0.4738	0.5686	0.6634
Δ (%)	10.09	6.13	5.56	5.90	4.99
Discrepancy Δ (%) = |Theoretical prediction – Average |/Average $\times$ 100%					

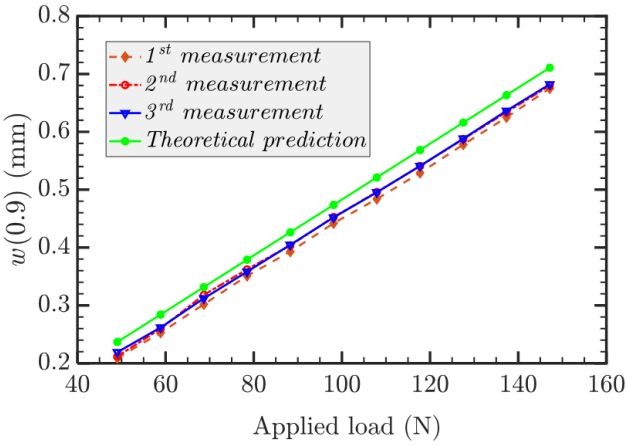

Figure 7. Comparison of the deflection between the theoretical prediction and experimental test

It is obvious from Table 3 and Fig. 7 that the test results are stable. The measurement results match well with the theoretical prediction.

b. Fundamental frequency

The measurement of the fundamental frequency for two cases of the test, i.e., excited by a rubber hammer or excited by cutting a weight hanging, is reported in Table 4. The FFT analysis to estimate the natural frequencies is illustrated in Fig. 8. It is clear that the test results are stable; the measurement results of the sets are nearly the same. The predicted frequency is also reported in Table 4. Notably, the discrepancy between the theoretical prediction and the average measurement results is just 5.24%.

Table 4. Comparison of the fundamental natural frequency between the theoretical prediction and experimental test ($f_1 = \omega_1/(2\pi)$ Hz)

Excited by a hammer			Excited by cutting a weight hanging			Average	Theoretical prediction	Δ (%)
1^{st}	2^{nd}	3^{rd}	1^{st}	2^{nd}	3^{rd}			
32.47	32.47	32.47	32.47	32.23	32.47	32.43	30.73	5.24
Discrepancy Δ (%) = |Theoretical prediction – Average |/Average × 100%								

c. Time history response

Finally, the deflection-time history of the beam at position $x = 0.9$ m (from the fix), excited by cutting a weight hanging of 10 kG, is measured and plotted in Fig. 9. Meanwhile, mesh-free analysis is also conducted to simulate the test for comparison. To capture more actual the response, the structural damping needs including in the analysis. Hence, Eq. (43) may be rewritten as [31]

$$\mathbf{M}\ddot{\mathbf{U}} + \mathbf{C}\dot{\mathbf{U}} + \mathbf{K}\mathbf{U} = \mathbf{F} \tag{45}$$

in which $\mathbf{C}$ is the damping matrix and $\dot{\mathbf{U}}$ is the velocity vector.

In this work, Rayleigh damping is adopted to estimate the structural damping. Thus, the damping matrix $\mathbf{C}$ can be expressed through the stiffness matrix $\mathbf{K}$ and mass matrix $\mathbf{M}$ by [31]

$$\mathbf{C} = a_0\mathbf{M} + a_1\mathbf{K} \tag{46}$$

Assuming that vibration modes have the same damping ratio ξ, the coefficients a_0 and a_1 can then be determined via the first two frequencies of the beam by [31]

$$\begin{Bmatrix} a_0 \\ a_1 \end{Bmatrix} = \frac{2\xi}{\omega_1 + \omega_2} \begin{Bmatrix} \omega_1\omega_2 \\ 1 \end{Bmatrix} \tag{47}$$

In addition, the damping ratio of the studied beam is $\xi \approx 5.93\%$. This value of the damping ratio is determined from the data of experiment results by the following equation [31]

$$\xi = \frac{1}{2\pi j} \ln \frac{w_i}{w_{i+j}} \tag{48}$$

where w_i and w_{i+j} are the deflection amplitude data of i-th and $(i + j)$-th cycles of the vibration, respectively.

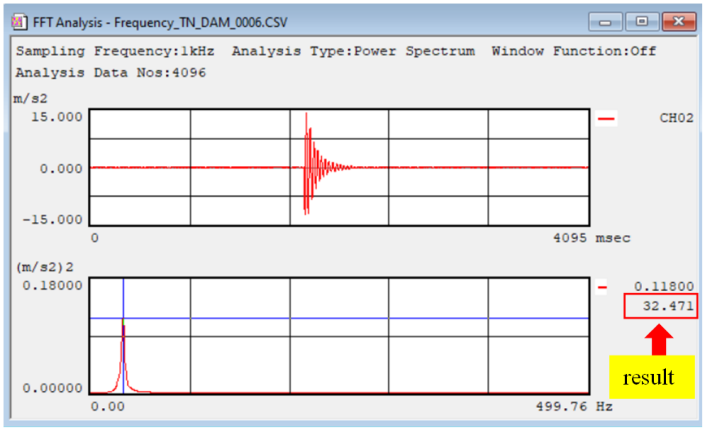

Figure 8. FFT analysis for the natural frequencies for the last test

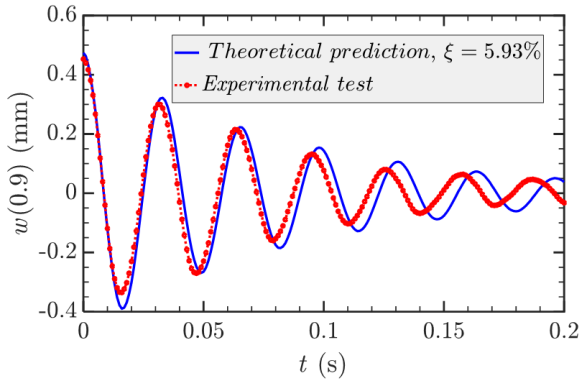

Figure 9. Comparison of the deflection-time history at $x = 0.9$ (m) between the theoretical prediction and experimental test

Eq. (45) is solved by the Newmark method [31] with constant acceleration and the time step 0.001 (s). The deflection-time history is plotted in Fig. 9. As shown in Fig. 9, the measurement of the vibration amplitudes matches well with the theoretical prediction. The time intervals between the peaks of the test are slightly shorter than those of the theoretical prediction. This feature is consistent with the frequency value given in Table 4. In other words, the greater frequency value results in the

shorter time period of the vibration and vice versa. Consequently, in later cycles, the distances the of the peaks in the figure become wider.

In summary, the static and dynamic behaviour of the porous sandwich beam measured by the experimental tests and those predicted by the mesh-free analysis are in good agreement. The relative difference between them is assessed and can be acceptable. These mismatches may be due to (i) the error in the measurements, and (ii) the discrepancy between the physical model for the theoretical prediction and the actual porous sandwich beam specimen.

5. Conclusions

In this paper, we investigate the static bending and vibration of sandwich beam with a porous core through the theoretical prediction and experimental tests. Mesh-free method based on moving least squares Hermite interpolation is developed to model 1D beams. To recover the Kronecker delta property of the constructed shape functions, a simple transformation method is employed. This allows us to impose the boundary conditions directly, similar to the FEM, without requiring additional techniques. The reliability of the developed method was verified with previous data in the literature. Subsequently, experimental tests were conducted on a cantilever porous sandwich beam to validate the theoretical predictions based on various mechanical responses, including natural frequency, static deflection, and deflection-time history. The obtained results indicate that (i) the developed mesh-free method is efficient, characterized by a high convergence rate in the solutions; (ii) the theoretical predictions align well with the experimental tests. Furthermore, the study results can serve as benchmarks for further research on the mechanical problems of porous sandwich beams.

Acknowledgement

This research is funded by Vietnam National Foundation for Science and Technology Development (NAFOSTED) under grant number 107.02-2021.16.

References

[1] Chen, D., Kitipornchai, S., Yang, J. (2016). Nonlinear free vibration of shear deformable sandwich beam with a functionally graded porous core. *Thin-Walled Structures*, 107:39–48.

[2] Wang, Y., Ma, H., Xie, K., Fu, T., Chen, J., Liu, Y. (2022). Nonlinear bending of a sandwich beam with metal foam and GPLRC face-sheets using Chebyshev–Ritz method: Effects of agglomeration and internal pore. *Thin-Walled Structures*, 181:110035.

[3] Srikarun, B., Songsuwan, W., Wattanasakulpong, N. (2021). Linear and nonlinear static bending of sandwich beams with functionally graded porous core under different distributed loads. *Composite Structures*, 276:114538.

[4] Magnucka-Blandzi, E. (2011). Dynamic Stability and Static Stress State of a Sandwich Beam with a Metal Foam Core Using Three Modified Timoshenko Hypotheses. *Mechanics of Advanced Materials and Structures*, 18(2):147–158.

[5] Wang, Y. Q., Zhao, H. L. (2019). Free vibration analysis of metal foam core sandwich beams on elastic foundation using Chebyshev collocation method. *Archive of Applied Mechanics*, 89(11):2335–2349.

[6] Garg, A., Chalak, H. D., Belarbi, M. O., Zenkour, A. M. (2022). A parametric analysis of free vibration and bending behavior of sandwich beam containing an open-cell metal foam core. *Archives of Civil and Mechanical Engineering*, 22(1).

[7] Wang, Y., Zhou, A., Fu, T., Zhang, W. (2019). Transient response of a sandwich beam with functionally graded porous core traversed by a non-uniformly distributed moving mass. *International Journal of Mechanics and Materials in Design*, 16(3):519–540.

[8] Chinh, T. H., Tu, T. M., Duc, D. M., Hung, T. Q. (2020). Static flexural analysis of sandwich beam with functionally graded face sheets and porous core via point interpolation meshfree method based on polynomial basic function. *Archive of Applied Mechanics*, 91(3):933–947.

[9] Hung, D. X., Truong, H. Q. (2018). Free vibration analysis of sandwich beams with FG porous core and FGM faces resting on Winkler elastic foundation by various shear deformation theories. *Journal of Science and Technology in Civil Engineering (STCE) - NUCE*, 12(3):23–33.
[10] Derikvand, M., Farhatnia, F., Hodges, D. H. (2021). Functionally graded thick sandwich beams with porous core: Buckling analysis via differential transform method. *Mechanics Based Design of Structures and Machines*, 51(7):3650–3677.
[11] Hung, T. Q., Duc, D. M., Tu, T. M. (2021). *Static Behavior of Functionally Graded Sandwich Beam with Fluid-Infiltrated Porous Core*. Springer Singapore, 691–706.
[12] Jasion, P., Magnucka-Blandzi, E., Szyc, W., Magnucki, K. (2012). Global and local buckling of sandwich circular and beam-rectangular plates with metal foam core. *Thin-Walled Structures*, 61:154–161.
[13] Sokolinsky, V. S., Shen, H., Vaikhanski, L., Nutt, S. R. (2003). Experimental and analytical study of nonlinear bending response of sandwich beams. *Composite Structures*, 60(2):219–229.
[14] Sokolinsky, V. S., Von Bremen, H. F., Lavoie, J. A., Nutt, S. R. (2004). Analytical and Experimental Study of Free Vibration Response of Soft-core Sandwich Beams. *Journal of Sandwich Structures & Materials*, 6(3):239–261.
[15] Dariushi, S., Sadighi, M. (2014). A new nonlinear high order theory for sandwich beams: An analytical and experimental investigation. *Composite Structures*, 108:779–788.
[16] Njim, E., Bakhi, S., Al-Waily, M. (2022). Experimental and Numerical Flexural Properties of Sandwich Structure with Functionally Graded Porous Materials. *Engineering and Technology Journal*, 40(1):137–147.
[17] Kitipornchai, S., Chen, D., Yang, J. (2017). Free vibration and elastic buckling of functionally graded porous beams reinforced by graphene platelets. *Materials & Design*, 116:656–665.
[18] Karamanlı, A. (2018). Free vibration analysis of two directional functionally graded beams using a third order shear deformation theory. *Composite Structures*, 189:127–136.
[19] Reddy, J. N. (2003). *Mechanics of Laminated Composite Plates and Shells*. CRC Press.
[20] Liu, G.-R. (2009). *Meshfree methods: moving beyond the finite element method*. CRC Press.
[21] Quang Hung, T., Duc, D. M., Minh Tu, T. (2022). Static bending mesh-free analysis of smart piezoelectric porous beam reinforced with graphene platelets. *Proceedings of the Institution of Mechanical Engineers, Part C: Journal of Mechanical Engineering Science*, 237(7):1595–1612.
[22] Hung, T. Q., Tu, T. M., Duc, D. M. (2022). Free vibration analysis of sandwich beam with porous FGM core in thermal environment using mesh-free approach. *Archive of Mechanical Engineering*, 69.
[23] Duc, D. M., Hung, T. Q., Tu, T. M. (2023). Analytical and mesh-free approaches to dynamic analysis and active control of smart FGP-GPLRC beam. *Structures*, 56:105020.
[24] Belytschko, T., Lu, Y. Y., Gu, L. (1994). Element-free Galerkin methods. *International Journal for Numerical Methods in Engineering*, 37(2):229–256.
[25] Cao, Y., Yao, L., Yin, Y. (2013). New treatment of essential boundary conditions in EFG method by coupling with RPIM. *Acta Mechanica Solida Sinica*, 26(3):302–316.
[26] Liu, G.-R., Gu, Y.-T. (2005). *An introduction to meshfree methods and their programming*. Springer Science & Business Media.
[27] Atluri, S. N., Kim, H.-G., Cho, J. Y. (1999). A critical assessment of the truly Meshless Local Petrov-Galerkin (MLPG), and Local Boundary Integral Equation (LBIE) methods. *Computational Mechanics*, 24(5):348–372.
[28] Atluri, S. N., Cho, J. Y., Kim, H.-G. (1999). Analysis of thin beams, using the meshless local Petrov-Galerkin method, with generalized moving least squares interpolations. *Computational Mechanics*, 24 (5):334–347.
[29] Spitzbart, A. (1960). A Generalization of Hermite's Interpolation Formula. *The American Mathematical Monthly*, 67(1):42–46.
[30] Prasittisopin, L., Termkhajornkit, P., Kim, Y. H. (2022). Review of concrete with expanded polystyrene (EPS): Performance and environmental aspects. *Journal of Cleaner Production*, 366:132919.
[31] Chopra, A. K. (2017). *Dynamics of structures: Theory and applications to Earthquake Engineering*.